IFRFNet: Iterative Frequency Restoration-Fusion Network for Fast System Matrix Calibration on Magnetic Particle Image

Weixin Xu[1,2,3], Penghua Zhai[1,2,3], Jie Tian[1,2]⋆ and Wei Mu[1,2,3]⋆⋆

[1]School of Engineering Medicine, Beihang University, Beijing, China
[2]Key Laboratory of Big Data-Based Precision Medicine (Beihang University), Ministry of Industry and Information Technology of the People's Republic of China, Beijing 100191, China
[3]Qingdao Research Institute, Beihang University, Qingdao 266100, China

Abstract. Magnetic Particle Imaging (MPI), an emerging technique with high sensitivity and resolution, requires time-consuming calibration for System Matrix (SM)-based reconstruction. Due to the strong locality and redundancy in the frequency domain, sparse sampling can capture sufficient information for rapid SM calibration without full-size SMs. However, it often leads to low-frequency energy leakage due to nonlinear magnetization of nanoparticles, causing the loss of low-frequency components. These components are essential for maintaining the SM's shape, and their absence leads to structural degradation and visible artifacts. Current methods tend to overemphasize high-frequency features, neglecting these low-frequency ones. Besides, single-step upsampling leads to error accumulation, especially with large scaling ratios, degrading reconstruction quality. To address these issues, we propose the Iterative Frequency Restoration-Fusion Network (IFRFNet), which uses an iterative frequency-domain restoration-fusion module. Unlike single-step upsampling, our approach refines, fuses, and upsamples high- and low-frequency features in stages, ensuring continuous optimization. This prevents error accumulation, preserves fine details, and maintains structural integrity. By iteratively recovering low-frequency components and refining high-frequency details, IFRFNet minimizes artifacts and retains crucial information. The Effective Upsampler further enhances the quality of the features, ensuring clear and realistic final SM volumes. Experiments on the OpenMPI dataset show that IFRFNet achieves SOTA performance.

Keywords: MPI · System Matrix · Fast Calibration.

This study was supported by the National Natural Science Foundation of China (62176013, 92259205, 62027901), Beijing Natural Science Foundation (L222021), National Key Research and Development Program of China (2022YFC2505100), Shandong Provincial Natural Science Foundation (ZR2024QF010), and the Science, Technology and Innovation Project of Xiongan New Area (2023XAGG0071).

⋆ Corresponding author: jie.tian@ia.ac.cn

⋆⋆ Corresponding author: weimu@buaa.edu.cn

1 Introduction

Magnetic Particle Imaging (MPI) is a tomographic imaging technique capable of detecting the magnetism of iron oxide nanoparticles injected into the bloodstream to produce three-dimensional images [9] [22]. In recent years, MPI has garnered significant attention for its ability to enhance imaging resolution without the use of radioactive substances. This technology has been extensively explored in various fields, including vascular imaging, cell tracking, tumor imaging, and has achieved remarkable progress in clinical translation. Traditionally, MPI reconstruction relies on two primary methods: X-space-based methods and system matrix (SM)-based methods [4]. Among these, the SM-based approach offers superior image quality but requires a highly complex and time-intensive calibration process. This process involves measuring the voxel-level response of the MPI scanner within the field of view (FOV) to generate a complex-valued SM. For instance, obtaining a system matrix of size $37 \times 37 \times 37$ can take approximately 32 hours, whereas a reduced size of $9 \times 9 \times 9$ requires only about 37 minutes. Sparse sampling has been proposed to accelerate the calibration process, as it can capture enough information for rapid SM calibration without the need for full-size SMs. Despite its advantages, sparse sampling often leads to low-frequency energy leakage due to the nonlinear magnetization of nanoparticles, which enables imaging but concentrates signal energy in high frequencies, leading low-frequency components relatively weak and easily suppressed [19]. Also, sparse sampling cannot fully cover all spatial points [14]. These low-frequency components are essential for preserving the overall shape and structure of the SM. Their absence can cause structural degradation and visible artifacts, compromising the quality of the reconstructed images. Recent approaches have addressed this issue by treating SM calibration as compressed sensing (CS) [10, 11, 14] and super-resolution (SR) methods [2, 12, 18] to reconstruct high-resolution images from low-resolution SMs acquired through rapid sparse calibration, accelerating the calibration process. With the rapid development of deep learning, many methods have been proposed for SR tasks. The SRCNN [5] was the pioneering deep learning model applied to image super-resolution (SR) using an end-to-end convolutional neural network (CNN). Since then, various CNN-based approaches [1, 6, 21] have been developed to address the SR problem. LKFN [3] enhances feature extraction by introducing larger kernel convolutions, thus providing a wider receptive field. SMFANet [20] proposes the SMFA module, which efficiently captures both non-local and local features to extract more representative information. Additionnally, some Vision Transformer (ViT) [7] based methods are proposed to complete variational tasks [8, 17]. TTVSR [17] presents a framework that incorporates both temporal consistency and spatial attention, significantly improving video super-resolution by capturing temporal and spatial dependencies efficiently. TranSMS [8] introduced a multi-scale transformer-based architecture that captures fine-grained details across multiple scales, enhancing the model's ability to perform 2D SM calibration in MPI.

However, these methods often prioritize high-frequency features at the expense of low-frequency components, leading to the neglect of essential structural information. Furthermore, single-step upsampling methods suffer from error accumulation, especially when scaling ratios are large (e.g., 4×), which results in the loss of fine details, increased artifacts, and difficulties in feature refinement. Finally, although iterative upsampling has proven that can effectively alleviate this problem [15], current methods often ignore further processing of the features after each upsampling step, directly using coarse features. If the features after each upsampling step are not fully optimized, the network may struggle to extract critical information, which in turn affects the clarity and authenticity of the final image. Additionally, errors from earlier stages can accumulate and be magnified in subsequent stages, ultimately degrading the overall super-resolution performance. To address the aforementioned challenges, we propose a novel fast SM calibration framework, named the Iterative Frequency Restoration-Fusion Network (IFRFNet). This framework employs an iterative frequency domain feature refine module that filters both high and low-frequency domain features while simultaneously repairing and fusing them. Subsequently, we utilize the Effective Upsampler to upsample and optimize the features, ensuring that the final calibrated SM volumes retain both clarity and reality, effectively restoring the overall shape.

Our main contributions are summarized as follows:

- We propose a novel attention-based frequency refinement module, termed the Frequency Attention Module, designed to capture both global and local features effectively. This module assigns varying weights to the extracted frequency features, ranging from 0 to 1, reflecting their relative importance.
- We propose a novel frequency domain feature processing module, consisting of the Frequency Filter and Frequency Refine-Fusion Module, to filter, refine, and fusion the features with different frequencies to help better restore the information gap between low-resolution SMs and high-resolution SMs.
- To better generate the high-resolution SMs from the low-resolution ones, we propose an Effective Upsampler module, which could effectively upsample restored frequency fusion features directly.
- Based on the Frequency Filter, Frequency Refine-Fusion Module, and Effective Upsampler, we propose a novel framework, for fast SM calibration on MPI, dubbed IFRFNet, which achieves state-of-the-art (SOTA) performance on the OpenMPI dataset, the widely used public benchmark with extensive resources for MPI research and development.

2 Methods

2.1 Overall Architecture

The overall architecture of our proposed IFRFNet is shown in Fig. 1. Specifically, our proposed IFRFNet consists of the following aspects: 1). The encoder, which is used to extract the shallow feature from low-resolution SM input, consists of two convolution blocks. 2). The iterative frequency restoration blocks. These blocks are imported to filter high and low frequencies from the previous encoder

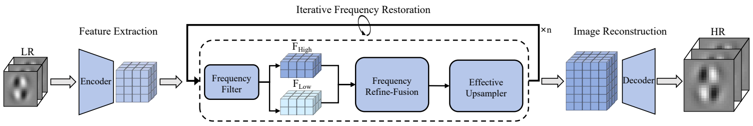

Fig. 1: The framework of our proposed IFRFNet.

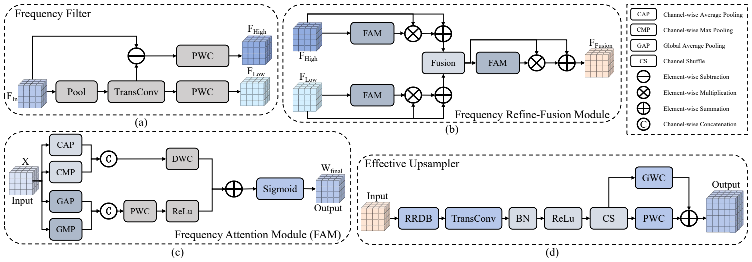

Fig. 2: Details about our proposed modules.

layer first, then refine those frequencies and fuse the more precise frequencies. Finally, an effective upsampler was proposed to upsample the refined frequencies to the needed sizes. The number of restoration blocks equals $\log_2 U$, in which U represents the upsampling ratio. 3). The decoder block was built by a single convolution block, to reconstruct features to the SMs with high resolution.

2.2 Frequency Filter

Following the feature extraction block, the Frequency Filter (FF) is proposed to split features with high frequency and low frequency, details of the FF are shown in Fig. 2 (a). Specifically, since the low frequency represents the overall shape of the inputs, we proposed to utilize the average pooling module first to extract the global shape information. Then, a transposed convolution is incorporated to recover the spatial resolution of the features. Finally, a point-wise convolution (PWC) is used to get the filtered low-frequency features, F_{Low}. Details of this process are shown in eq. 1.

$$F_{Low} = PWC(TransConv(Pool(F_{In}))) \tag{1}$$

Moreover, as shown in the eq. 2, for the high-frequency features that focus on detailed texture information, we use element subtraction to subtract the low-frequency features before PWC from input features, which can effectively remove the overall shape information and separate the high-frequency features. Afterward, similar to the low-frequency filter, we used a PWC operation to get the final high-frequency features, dubbed F_{High}.

$$F_{High} = PWC(F_{In} - TransConv(Pool(F_{In}))) \tag{2}$$

2.3 Frequency Refine-Fusion Module

To refine and fusion the filtered frequency-domain features, we propose the Frequency Refine-Fusion Module (FRFM), details are shown in Fig. 2 (b). This module consists of two main blocks: Frequency Attention Module (FAM), details are shown in Fig. 2 (c), and Fusion block. Specifically, for the input frequency-domain features, F_{High} and F_{Low}, a FAM was first used to calculate the weights for each feature. After the weights are calculated, it is multiplied with the input frequency feature to obtain a feature map with different importances, and the skip connection is used to add it to the original feature map to obtain the final refined frequency domain feature map that retains the context information. We adopt the FAM on F_{High}, F_{Low} and the fused coarse features, therefore get F^f_{High}, F^f_{Low}, F^f_{Fusion}.

FAM: To effectively capture both global and local information across channel and spatial dimensions, we propose a two-step attention mechanism on input frequency-domain feature X. First, we introduce channel-wise attention to compute attention weights along the channel dimension. This involves two operations: channel average pooling (CAP) and channel max pooling (CMP). Specifically, the resulting channel-wise vectors, $W_{ca} \in \mathbb{R}^{C\times1\times1\times1}$ and $W_{cm} \in \mathbb{R}^{C\times1\times1\times1}$, represent global and local features, respectively. These two vectors are then concatenated to obtain the combined channel-wise attention weights. Finally, we apply a depth-wise convolution (DWC) to generate the final channel attention output, denoted W_c, details of this process are shown in eq. 3. Moreover, for the spatial dimensions, we utilize global average pooling (GAP) and global max pooling (GMP) to compute spatial attention vectors, $W_{sa} \in \mathbb{R}^{1\times H\times W\times D}$ and $W_{sm} \in \mathbb{R}^{1\times H\times W\times D}$, which capture global and local spatial features, respectively. These features are concatenated, and a PWC with a ReLU activation is applied to generate the final spatial attention output, W_s, details of this process are shown in eq. 4.

$$W_c = DWC(Concat(CAP(x), CMP(x))) \tag{3}$$

$$W_s = ReLu(PWC(Concat(GAP(x), GMP(x)))) \tag{4}$$

After obtaining the channel attention weights W_c and spatial attention weights W_s, we combine them through element-wise addition $W = W_c + W_s$, followed by a sigmoid activation $W_{final} = \sigma(W)$ to normalize the values between 0 and 1. This operation ensures a balanced contribution from both channel and spatial attention, improves feature selection by focusing on relevant features, and stabilizes the learning process through normalization.

Fusion Block: To achieve effective feature integration from high-frequency and low-frequency representations, we utilize a simple yet effective fusion block. This block enables the integration of high-frequency and low-frequency features and preserves complementary information from both inputs by splitting the features and performing separate additions. Specifically, given two inputs $F^f_{\text{High}} \in \mathbb{R}^{C\times H\times W\times D}$ and $F^f_{\text{Low}} \in \mathbb{R}^{C\times H\times W\times D}$, we first split each input along the channel dimension into two equal parts:

$$F^{f,1}_{\text{High}}, F^{f,2}_{\text{High}} = F^f_{\text{High}}[: C/2, :, :, :], \quad F^{f,1}_{\text{Low}}, F^{f,2}_{\text{Low}} = F^f_{\text{Low}}[: C/2, :, :, :] \tag{5}$$

Next, we perform element-wise addition on the corresponding parts:

$$F^{f,1} = F^{f,1}_{\text{High}} + F^{f,1}_{\text{Low}}, \quad F^{f,2} = F^{f,2}_{\text{High}} + F^{f,2}_{\text{Low}} \tag{6}$$

Finally, the fused output F^f_{out} is obtained by concatenating $F^{f,1}$ and $F^{f,2}$ along the channel dimension:

$$F^f_{\text{out}} = \text{Concat}(F^{f,1}, F^{f,2}), \quad F^f_{\text{out}} \in \mathbb{R}^{C \times H \times W \times D} \tag{7}$$

2.4 Effective Upsampler

The proposed Effective Upsampler, as depicted in Fig. 2 (d), is a carefully designed module aimed at enhancing the resolution of input feature maps while maintaining high-quality feature representation. The process begins with an input feature map passing through a Residual-in-Residual Dense Block (RRDB) [23], which effectively captures both local and global context features. Following this, a transposed convolution layer (TransConv) performs upsampling to increase the spatial resolution. Batch normalization (BN) and ReLU activation are applied to stabilize the training process and introduce non-linearity, respectively. Subsequently, a Channel Shuffle (CS) operation reorganizes feature channels to enhance feature interaction, followed by two parallel pathways. The first pathway applies a Group-Wise Convolution (GWC) layer to assign channel-specific features adaptively, while the second pathway utilizes a PWC to refine spatial details. Finally, the outputs of the two pathways are element-wise summed, resulting in the final upsampled feature map.

3 Experiments

3.1 Dataset

The OpenMPI dataset [13], the first open-source MPI dataset, has become a widely used public benchmark with extensive resources to support MPI research and development. This dataset includes system matrix (SM) calibration data and phantom measurements derived from various magnetic nanoparticle (MNP) formulations. Following standard practices [2], we specifically utilized Experiment #7 of the SM calibration, which features SynomagD MNPs (Micromod GmbH, Germany), to construct our training dataset. For testing, we used Experiment #6, which includes Perimag MNP (Micromod GmbH, Germany), to assess the generalizability of the model across different types of MNP. To ensure the reliability and robustness of our experimental results, we applied stringent filtering criteria, retaining only SMs with a signal-to-noise ratio (SNR) greater than 3. This preprocessing step produced a training set of 4,129 volumes and a test set of 3,290 volumes.

3.2 Implementation Details

Our experimental setup utilized PyTorch version 1.13.1 for all model training. The training process was executed on a single NVIDIA RTX 4090 GPU equipped with 24GB of memory. The models were optimized using the Adam optimizer, initialized with a learning rate of 2.5×10^{-4}, a decay factor of 0.2, and a weight

Table 1: SM calibration results on OpenMPI dataset, with the best performing values in bold and the second best performing values underlined.

Ratio	2×	4×
Method	nRMSE↓ (%)	nRMSE↓ (%)
Bicubic	6.76	8.76
Trilinear	6.21	8.55
SRCNN [5]	3.88	5.70
3dSMRnet [2]	<u>3.62</u>	<u>4.86</u>
VolumeNet [16]	4.13	6.12
SMFANet [20]	4.04	5.81
LKFN [3]	3.98	6.02
Ours	**3.47**	**4.62**

decay of 5×10^{-4}. Following the methodology outlined in [8], we adopted the L1 loss function, mathematically expressed as:

$$L_1 = \frac{1}{N} \sum_{i=1}^{N} |y_i - \hat{y}_i|, \tag{8}$$

where N denotes the total number of samples, y_i represents the ground truth values, and $\hat{y}_i$ refers to the predicted outputs.

3.3 Evaluation Metrics

We utilized three widely recognized metrics to quantitatively evaluate the performance of various state-of-the-art (SOTA) models. Following the approach adopted in prior studies [2,8], the normalized Root Mean Square Error (nRMSE) was employed as the sole metric for SM calibration assessment. For image reconstruction evaluation, we used nRMSE alongside Peak Signal-to-Noise Ratio (PSNR) and Structural Similarity Index Measure (SSIM).

3.4 Results

We evaluated our approach against seven SOTA models: Bicubic interpolation, Trilinear interpolation, SRCNN, 3dSMRnet, VolumeNet, SMFANet, and LKFN. The evaluation followed a two-step process. In the first step, we measured the accuracy of the reconstructed SMs by comparing them to the ground truth. In the second step, we utilized the calibrated SMs to reconstruct the measurements of the shape and resolution phantoms in OpenMPI dataset. For consistency, the same standard regularization parameter was applied ($\lambda = 0.75$) across three iterations.

SM Calibration Results The quantitative results of the SM calibration are summarized in Table 1. Notably, with a scaling ratio equals 2, the proposed IFRFNet demonstrates a remarkable improvement by reducing the normalized Root Mean Square Error (nRMSE) by 0.15% compared to prior state-of-the-art (SOTA) approaches. This notable enhancement underscores the accuracy

Table 2: Image reconstruction results of Resolution phantom on calibrated SM on OpenMPI dataset, with the best performing values in bold and the second best performing values underlined.

Ratio	2×			4×		
Method	nRMSE(↓)	PSNR(↑)	SSIM(↑)	nRMSE(↓)	PSNR(↑)	SSIM(↑)
Bicubic	1.93%	34.31	0.8960	8.49%	21.42	0.2181
Trilinear	1.86%	34.60	0.8634	9.64%	20.31	0.1474
SRCNN	0.78%	42.17	0.9553	5.81%	24.71	0.2374
3dSMRnet	0.75%	42.48	0.9569	2.64%	31.58	0.6201
VolumeNet	0.77%	42.28	0.9556	6.54%	23.69	0.233
SMFANet	0.77%	42.24	0.9559	5.74%	24.81	0.2482
LKFN	0.73%	42.71	0.9585	5.66%	24.94	0.2241
Ours	**0.72%**	**42.82**	**0.9589**	**2.24%**	**33.00**	**0.7004**

Table 3: Image reconstruction results of Shape phantom on calibrated SM on OpenMPI dataset, with the best performing values in bold and the second best performing values underlined.

Ratio	2×			4×		
Method	nRMSE(↓)	PSNR(↑)	SSIM(↑)	nRMSE(↓)	PSNR(↑)	SSIM(↑)
Bicubic	3.19%	29.93	0.8106	8.45%	21.46	0.3902
Trilinear	3.12%	30.12	0.7968	7.03%	23.06	0.3265
SRCNN	1.51%	36.43	0.8716	4.61%	26.72	0.4813
3dSMRnet	1.57%	36.11	0.8589	2.90%	30.75	0.6815
VolumeNet	1.50%	36.46	0.8742	5.48%	25.22	0.4241
SMFANet	1.48%	36.58	0.8768	5.48%	25.23	0.4367
LKFN	1.49%	36.56	0.8761	5.56%	25.10	0.4385
Ours	**1.45%**	**36.78**	**0.8781**	**2.58%**	**31.78**	**0.7014**

and robustness of IFRFNet in addressing moderate scaling ratios. Furthermore, when the scaling ratio increased to 4, IFRFNet consistently maintains its superior performance, achieving an additional 0.24% reduction in nRMSE. These results highlight the versatility and adaptability of IFRFNet across varying scaling ratios, reaffirming its advantage over existing methodologies.

Image Reconstruction Results We evaluated the image reconstruction performance using a super-resolution calibrated SM. For image reconstruction, following [2], we selected the shape phantom and resolution phantom from the OpenMPI dataset. Quantitative results of these two phantoms are shown in table 2 and 3. Similar to results in table 1, results of image reconstruction and SM calibration are almost consistent. Specifically, for the resolution phantom, compared with the previous SOTA methods, performance of our proposed IFRFNet can achieve (0.01%, 0.11, 0.0004) improvement on (nRMSE, PSNR, SSIM) metrics when the scaling ratio equals 2 and (0.40%, 1.42, 0.0803) improvement on (nRMSE, PSNR, SSIM) metrics for ratio 4. Moreover, for the shape phantom, compared with the previous SOTA methods, performance of our proposed IFRFNet can achieve (0.04%, 0.21, 0.0013) improvement on (nRMSE, PSNR, SSIM) metrics when the scaling ratio equals 2 and (0.32%, 1.03, 0.0199) improvement on (nRMSE, PSNR, SSIM) metrics for ratio 4.

4 Conclusion

In this paper, we present a novel and efficient SM calibration framework for MPI, termed IFRFNet. The proposed model employs the iterative strategy to enhance the restoration of shape and resolution information in SM by effectively filtering high- and low-frequency features and optimizing their fusion through an attention-based mechanism. To achieve this, we first introduce a Frequency Filter Module, which isolates low- and high-frequency features from the original inputs. Next, we propose the Frequency Refine-Fusion Module, the core of which includes the Frequency Attention Module (FAM) and the Fusion Block. FAM help to refine the high- and low-frequency features extracted in the previous stage, while a dedicated Fusion Block integrates the optimized features more effectively. Finally, an Effective Upsampler is designed to further refine features during the upsampling process, mitigating issues such as uneven feature distribution and cumulative error amplification. Experimental results on the OpenMPI dataset demonstrate that IFRFNet surpasses existing methods, avoiding loss of low-frequency information during upsampling. This work establishes a strong foundation for future advancements and practical applications in MPI.

Disclosure of Interests. We have no conflicts of interest to disclose.

References

1. Ahn, N., Kang, B., Sohn, K.A.: Fast, accurate, and lightweight super-resolution with cascading residual network. In: Proceedings of the European conference on computer vision (ECCV). pp. 252–268 (2018)
2. Baltruschat, I.M., Szwargulski, P., Griese, F., Grosser, M., Werner, R., Knopp, T.: 3d-smrnet: Achieving a new quality of mpi system matrix recovery by deep learning. In: Medical Image Computing and Computer Assisted Intervention–MICCAI 2020: 23rd International Conference, Lima, Peru, October 4–8, 2020, Proceedings, Part II 23. pp. 74–82. Springer (2020)
3. Chen, J., Duanmu, C., Long, H.: Large kernel frequency-enhanced network for efficient single image super-resolution. In: Proceedings of the IEEE/CVF Conference on Computer Vision and Pattern Recognition. pp. 6317–6326 (2024)
4. Chen, X., Jiang, Z., Han, X., Wang, X., Tang, X.: Research of magnetic particle imaging reconstruction based on the elastic net regularization. Biomedical Signal Processing and Control **69**, 102823 (2021)
5. Dong, C., Loy, C.C., He, K., Tang, X.: Image super-resolution using deep convolutional networks. IEEE transactions on pattern analysis and machine intelligence **38**(2), 295–307 (2015)
6. Dong, C., Loy, C.C., Tang, X.: Accelerating the super-resolution convolutional neural network. In: Computer Vision–ECCV 2016: 14th European Conference, Amsterdam, The Netherlands, October 11-14, 2016, Proceedings, Part II 14. pp. 391–407. Springer (2016)
7. Dosovitskiy, A., Beyer, L., Kolesnikov, A., Weissenborn, D., Zhai, X., Unterthiner, T., Dehghani, M., Minderer, M., Heigold, G., Gelly, S., et al.: An image is worth 16x16 words: Transformers for image recognition at scale. arXiv preprint arXiv:2010.11929 (2020)

8. Güngör, A., Askin, B., Soydan, D.A., Saritas, E.U., Top, C.B., Çukur, T.: Transms: Transformers for super-resolution calibration in magnetic particle imaging. IEEE Transactions on Medical Imaging **41**(12), 3562–3574 (2022)
9. Han, X., Li, Y., Liu, W., Chen, X., Song, Z., Wang, X., Deng, Y., Tang, X., Jiang, Z.: The applications of magnetic particle imaging: From cell to body. Diagnostics **10**(10), 800 (2020)
10. Ilbey, S., Top, C.B., Güngör, A., Çukur, T., Saritas, E.U., Güven, H.E.: Fast system calibration with coded calibration scenes for magnetic particle imaging. IEEE transactions on medical imaging **38**(9), 2070–2080 (2019)
11. Kaethner, C., Erb, W., Ahlborg, M., Szwargulski, P., Knopp, T., Buzug, T.M.: Non-equispaced system matrix acquisition for magnetic particle imaging based on lissajous node points. IEEE transactions on medical imaging **35**(11), 2476–2485 (2016)
12. Kluth, T., Bathke, C., Jiang, M., Maass, P.: Joint super-resolution image reconstruction and parameter identification in imaging operator: analysis of bilinear operator equations, numerical solution, and application to magnetic particle imaging. Inverse Problems **36**(12), 124006 (2020)
13. Knopp, T., Szwargulski, P., Griese, F., Gräser, M.: Openmpidata: An initiative for freely accessible magnetic particle imaging data. Data in brief **28**, 104971 (2020)
14. Knopp, T., Weber, A.: Sparse reconstruction of the magnetic particle imaging system matrix. IEEE transactions on medical imaging **32**(8), 1473–1480 (2013)
15. Lai, W.S., Huang, J.B., Ahuja, N., Yang, M.H.: Deep laplacian pyramid networks for fast and accurate super-resolution. In: Proceedings of the IEEE conference on computer vision and pattern recognition. pp. 624–632 (2017)
16. Li, Y., Iwamoto, Y., Lin, L., Xu, R., Tong, R., Chen, Y.W.: Volumenet: A lightweight parallel network for super-resolution of mr and ct volumetric data. IEEE Transactions on Image Processing **30**, 4840–4854 (2021)
17. Liu, C., Yang, H., Fu, J., Qian, X.: Learning trajectory-aware transformer for video super-resolution. In: Proceedings of the IEEE/CVF conference on computer vision and pattern recognition. pp. 5687–5696 (2022)
18. Omer, O.A., Wojtczyk, H., Buzug, T.M.: Simultaneous reconstruction and resolution enhancement for magnetic particle imaging. IEEE Transactions on Magnetics **51**(2), 1–4 (2015)
19. Panagiotopoulos, N., Duschka, R.L., Ahlborg, M., Bringout, G., Debbeler, C., Graeser, M., Kaethner, C., Lüdtke-Buzug, K., Medimagh, H., Stelzner, J., et al.: Magnetic particle imaging: current developments and future directions. International journal of nanomedicine pp. 3097–3114 (2015)
20. Ren, B., Li, Y., Mehta, N., Timofte, R., Yu, H., Wan, C., Hong, Y., Han, B., Wu, Z., Zou, Y., et al.: The ninth ntire 2024 efficient super-resolution challenge report. In: Proceedings of the IEEE/CVF Conference on Computer Vision and Pattern Recognition. pp. 6595–6631 (2024)
21. Sun, L., Dong, J., Tang, J., Pan, J.: Spatially-adaptive feature modulation for efficient image super-resolution. In: Proceedings of the IEEE/CVF International Conference on Computer Vision. pp. 13190–13199 (2023)
22. Sun, S., Chen, Y., Zhao, M., Xu, L., Zhong, J.: Image reconstruction for magnetic particle imaging based on sparse representation and deep learning. IEEE Transactions on Instrumentation and Measurement **73** (2024)
23. Wang, X., Yu, K., Wu, S., Gu, J., Liu, Y., Dong, C., Qiao, Y., Change Loy, C.: Esrgan: Enhanced super-resolution generative adversarial networks. In: Proceedings of the European conference on computer vision (ECCV) workshops (2018)